*Journal of Applied Fluid Mechanics*, Vol. 12, No. 6, pp. 1729-1744, 2019.
Available online at www.jafmonline.net, ISSN 1735-3645, EISSN 1735-3645.
DOI: 10.29252/jafm.12.06.29742

# Application of Lobed Mixers to Reduce Drag of Boat-Tailed Ground Vehicles

A. A. Rejniak† and A. Gatto

*Brunel University London, Uxbridge, UB8 3PH, United Kingdom*

†*Corresponding Author Email: aleksandra.rejniak@brunel.ac.uk*

(Received October 15, 2018; accepted January 23, 2019)

## ABSTRACT

Minimising the aerodynamic drag of commercial vehicles is important economically and ecologically. This work demonstrates the effective use of lobed-mixing geometries, traditionally used to enhance flow mixing, as a viable, passive flow control method for reducing base pressure drag of boat-tailed ground vehicles. Experiments were performed on a 1/24$^{th}$-scale Heavy Goods Vehicle representative model at a Reynolds number of $2.3 \times 10^5$ with force and hot-wire anemometry measurements used to quantify drag and wake characteristics. Tests on a baseline (no boat-tail), an unaltered boat-tail, and lobed-mixing configurations with varying pitch and height were compared. Overall, the baseline and unaltered boat-tail exhibited good correlation to previous results. This provided confidence in the methodology adopted. Results using lobed mixers showed up to a 10.2% drag reduction with the added vorticity produced acting to fundamentally shift the nature of the wake. This is manifested principally through the generation of counter-rotating vortical structures which enhance crosswise flow entrainment into the base wake. This action is observed to limit flow entrainment towards the ground leading to a higher wake and a characteristic 'waist'. Enhanced mixing is also demonstrated. Overall, results suggest the suitability of lobed mixers as an effective means for drag reduction of boat-tailed ground vehicles.

**Keywords**: Drag reduction; Lobed mixers; Boat-tailed vehicles.

## NOMENCLATURE

| | |
|---|---|
| b | boat-tail length normal to base |
| BT | Standard Boat-tail |
| C | geometry-dependent constant |
| $C_D$ | drag coefficient |
| h | crest-trough height of lobed mixer profile |
| H | height of model |
| HGV | Heavy Goods Vehicle |
| K | turbulence kinetic energy normalised by $1/(U_\infty)^2$ |
| $\overline{K}$ | average K |
| L | length of model |
| LB1-3 | Lobed Boat-tails 1-3 |
| p | pitch of lobed mixer profile |
| $Re_W$ | Reynolds Number based on width |
| $U_\infty$ | freestream velocity |
| $\overline{U}$ | axial velocity at lobe exit |
| v | velocity in Y-direction |
| VG | Vortex Generator |
| W | width of model |
| α | boat-tail angle |
| β | penetration angle |
| Δ | change |
| ω | velocity in Z-direction |
| Ω | vorticity magnitude normalised by $W/U_\infty$ |
| $\overline{\Omega}$ | non-normalised vorticity magnitude |

**Subscripts**

| | |
|---|---|
| X,Y,Z | streamwise, crosswise and heightwise directions |

## 1. INTRODUCTION

Transport using Heavy Goods Vehicles (HGVs) is a critical global enterprise. At highways speeds, up to 50% of the fuel consumed is used to overcome aerodynamic drag (Hucho and Sovran 1993). In 2016, 2.1 billion gallons of fuel were consumed by HGVs (Department for Transport UK 2017a, b), representing 22 million tonnes of $CO_2$ emitted into the atmosphere (ICBE 2000); equivalent to approximately 17% of total UK transport. Given

this scope, methods to reduce drag are eagerly sought. Particular interest resides in the base region, or rear of the trailer, which accounts for between 30% and 35% of total vehicle drag (Pankajakshan *et al.* 2010; van Raemdonck and van Tooren 2010). In this area, the separation from the blunt trailing edges form a large wake immediately behind the vehicle, which produces lower static pressures acting to resist vehicle motion. This region will be the focus of this paper.

Perhaps the most well-known legacy base drag reduction concept is the boat-tail. Typically, this device is installed at the rear of the trailer and incorporates a reducing cross-sectional area to better streamline the vehicle. Full-length boat-tails have shown drag reductions of up to 35% (Saltzman and Meyer, Jr. 1999), however, continue to remain somewhat impractical due to loading/unloading requirements and unsympathetic regulatory requirements. These limitations subsequently led to the development of a revised, truncated boat-tail, which provides almost the same benefit (34% - Saltzman and Meyer, Jr. 1999). Unfortunately however, both are yet to gain widespread use.

Attempts to optimise and realise operational boat-tails led to further concept developments. *Lanser et al.* (1991) conducted tests on straight-walled rear cavities, finding a 9.8% wind-averaged drag reduction; a result primarily due to higher base pressure development. The authors describe the cavity sides shielding the base from the normally lower wake pressures as the main mechanism. This is manifested by the entrapment of vortices between base edges and outer-cavity surfaces, leading to outer surface pressure reductions but inner-cavity pressure increases; the net effect being reduced drag. Several later studies also focused on boat-tailed cavities and flaps (Altaf *et al.* 2014; Martín-Alcántara *et al.* 2014; Salati *et al.* 2015; Kehs *et al.* 2013; Schaut and Sengupta 2015; Cooper 2003; Grover and Visser 2006; Howell *et al.* 2012; Pankajakshan *et al.* 2010; van Raemdonck and van Tooren 2010). Cooper (2003) shows that in combination with trailer skirts, adding a boat-tail has the potential to save up to 4000 US gallons of fuel per vehicle annually. Grover and Visser (2006) also noted fuel savings (approximately 10%) with optimum top and side flaps angled at 15° (bottom flap at 7°). This configuration also enhanced vehicle stability. Similarly, later work by Salati et al. (2015) has shown up to a 9% drag reduction with a boat-tail angle of 13°.

The generation of streamwise vorticity has long been used as a mechanism for drag reduction. Vortex generators (VG) remain a popular choice for this purpose, suppressing or delaying separation when required. Such devices generally work by enhancing the mixing process, modifying the near-boundary layer flow to allow greater tolerance of adverse pressure gradients. In many cases, while drag is increased locally, overall wake size dimensions reduce, resulting in a net benefit. For general aeronautical applications, Pujals *et al.* (2010) has shown VG effectiveness is greater when induced streamwise vortices are counter-rotating rather than co-rotating. Duriez *et al.* (2006) and Park *et al.* (2006) show up to a 20% decrease in wake size and increases in base pressure by 33% when VGs are used. For ground vehicles, Wood (2006) studied strake-like VGs on HGVs, which created localised vorticity, energising the flow near the trailer base edges. An improvement in fuel economy of 1% – 5% is reported together with enhanced wake stabilisation. Lav (2013), using delta-shaped VGs, noted similar improvements, with a drag reduction of 9.1%. While showing some promise however, such devices normally develop high induced drag, and to date, have achieved only limited operational use.

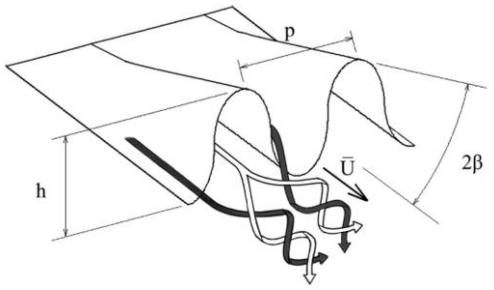


**Fig. 1. Schematic of a lobed mixer.**

Another common method to enhance mixing is through the use of lobed mixers. A lobed mixer is characterised as a three-dimensional, convoluted splitter plate, normally mounted upstream, with initially separate side flows. A basic schematic of a lobed mixer geometry is presented in Fig. 1 (depicted with an open end upstream). The principle of operation resides in mixing augmentation via an increase in interface area and the introduction of strong streamwise vorticity; the former through increasing the net surface area of flow interaction (equivalent to mixing the same volume of fluid over a larger surface) and the latter, via the increase in interfacial area gradients through strain. Production of streamwise vorticity is inherently linked to the penetration angle (hereafter defined as half of the streamwise subtended angle between lobe crests and troughs), with larger angles normally resulting in higher rates of interfacial length downstream growth (Waitz *et al.* 1997). Both Skebe *et al.* (1988) and Waitz *et al.* (1997), characterise the generation of streamwise vorticity, with Skebe *et al.* (1988) suggesting average lobe vorticity is given by:

$$\bar{\Omega}_X = (C\bar{U} \tan \beta) / p \quad (1)$$

Where C is a geometry-dependent constant, $\bar{U}$, the axial velocity at lobe exit, (Waitz et al. (1997) use the average of upstream velocities either side of the mixer), β, the penetration angle, and p, the pitch of the lobed profile. Skebe *et al.* (1988), Waitz *et al.* (1997), and Mao *et al.* (2009) also suggest that most effective mixing is achieved with a lobed profile with parallel sides due to stronger circulation potential and boundary layer blockage prevention in the troughs; in this case

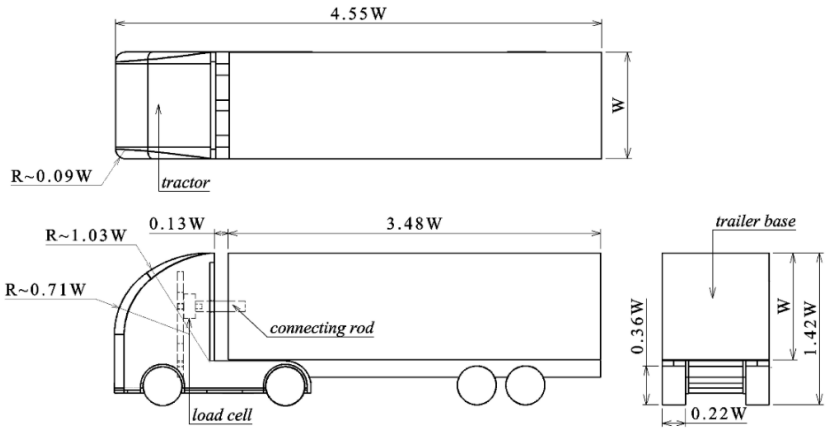


**Fig. 2. Schematic of the baseline model.**

C=1 is suggested by Waitz *et al.* (1997). The constant, C, is normally considered a comparative metric by which different lobe profile effectiveness can be assessed. For sinusoidal profiles, the value (in Eq. (1)) is within 0<C<1 with estimates made typically through inviscid analysis (Skebe *et al.* 1988). Such lobed mixers are particularly popular in the study of fuel injectors, as well as core-bypass mixing for jet engine noise reduction (Waitz *et al.* 1997; Depuru Mohan *et al.* 2015; Smith *et al.* 1997; Mao *et al.* 2006, 2009; McCormick and Bennett 1994; Yu and Yip 1997). Other applications have included base pressure drag reduction for projectile-like bluff bodies (Howard and Goodman 1985; Paterson *et al.* 1989) and more recently, modifying the reattachment length within transonic and supersonic flows (Bolgar *et al.* 2016; Schreyer and Taskin 2018).

With the use of lobed mixers becoming more widespread within the aeronautical field, application to automotive aerodynamics, specifically drag reduction, appears yet to be considered. Given the inherent capability of these devices to improve freestream flow/wake mixing thereby enhancing pressure recovery (with commensurate reductions in drag), their application to ground vehicles is appealing. This work investigates that application. Of primary focus is application within the base region of a small-scale, representative HGV. First, efforts centre on verifying the test setup on a baseline (no device fitted) and legacy boat-tail device to provide confidence in the methodology adopted. Several different lobed mixing geometries are thereafter assessed, compared, and evaluated.

## 2. EXPERIMENTAL SETUP AND APPARATUS

### 2.1 The Model

The simplified 1/24$^{th}$-scale model used for all experiments is shown in Fig. 2. This baseline model, representative of a HGV, neglects fine detail and incorporates a streamlined front face based on the Global Transportation System (GTS) model (Storms *et al.* 2001) to reduce the possibility of premature separation. It is constructed in two parts; a tractor and trailer bottom section, and the trailer. Overall dimensions are 500 mm long (L), 156 mm high (H), and 110 mm wide (W). The trailer is attached to the tractor as a separate section via a load cell and sliding contacts to allow the trailer to 'free-float' on the trailer bottom. This configuration allowed measurement of trailer drag with the base removable to allow installation of different inserts (see Fig. 3). The value of baseline total drag was measured separately using a rear-mounted support sting.

The model was made from Perspex and Aluminum with fully rotating wheels. The surface roughness of all elements was 'smooth'. The wheels were mounted on steel axles with installed ball bearings to ensure free rotation. Two 90° metal supports were mounted to the front of the tractor to locate and secure the model inside the wind tunnel test section (see Fig. 4). This atypical mounting was chosen to ensure minimal disruption of the wake flow at the base; downstream wakes from traditional mounting (i.e. from the sides or top of the model via support stings) were considered too intrusive to lobed mixer operation. Supports were fixed to an upstream flow splitter installed in the test section which acted to reduce the upstream boundary layer thickness. The splitter leading edge is 0.36 m from the model front face. Power and signal cables from the load cell were channeled through one of the front supports and flow splitter, and out of the test section. Perforated holes on the top splitter surface allowed application of suction to further aid boundary layer suppression.

### 2.2 Base Inserts

Four inserts in addition to the baseline (no insert) were studied; an unmodified boat-tail (BT) and 3 different lobe configurations (LB1, LB2, LB3). The various lobed mixer geometries are quantified in Fig. 3 and Table 1, together with the boat-tail used. All inserts have blunt trailing edges and identical overall streamwise length, b = 0.25W. Only lobed mixer profiles with parallel sides were chosen for this study, owing to their potential for higher

vorticity generation, and lower boundary layer blockage (Skebe *et al.* 1988; Mao *et al.* 2009). For the three lobed profiles tested, pitch (p), crest-trough height (h), and penetration angle (β) were varied. Each of these parameters were common to at least two devices to facilitate isolation of the influence on mixing and drag. A maximum boat-tail angle of α = 17° was selected for all four inserts allowing direct comparisons of performance. This angle is in general agreement to the optimum observed by Grover and Visser (2006). At full-scale, estimates made of the added weight due to the inclusion of such lobed profiling (Gross Vehicle Mass of 44 tonnes - Butcher (2009)) were less than 0.4% more than a standard boat-tail with the same overall dimensions and material specifications.

## 2.3 Wind Tunnel

All tests were conducted in an open-circuit wind tunnel with a closed test section measuring 1.3 m long, 0.46 m wide, and 0.36 m high. A moving belt of width 0.36 m is used to simulate the influence of a moving ground. A schematic is shown in Fig. 4. Based on projected frontal area, the blockage is 10.3%, which remains below the limit of 15% suggested for comparative testing in SAE J1252 (SAE International 2012). The freestream uniformity, turbulence intensity, and heightwise velocity consistency at a central test section (empty) position are ±1%, 0.5%, and within $\pm 0.05U_\infty$ (0.09W above the moving ground) respectively.

All tests were conducted at a freestream velocity of $U_\infty$ = 30 m/s, giving a Reynolds number based on body width of $Re_W = 2.3 \times 10^5$. This Reynolds number is low compared to full scale ($\approx 10^6$), however, the primary purpose of this work is to provide an initial performance assessment prior to subsequent analysis at larger scale. During operation, the speed of the belt was matched manually to the freestream within ±1 m/s, with the moving ground precipitating wheel rotation; a condition which has been noted to provide a better representation of drag and wake dynamics (Krajnović and Davidson 2005; Strachan *et al.* 2007). Suction was applied through a perforated plate located underneath the moving belt (to prevent inadvertent lifting during operation) with the setup driven by a 3 kW AC motor. The setup is monitored by LabVIEW control software with cooling water circulated throughout the perforated plate to facilitate better heat rejection.

## 2.4 Load Cell

For this work, trailer drag is measured. The load cell used is a Model 31 single axis tension/compression load cell by RDP Electronics. The mounting position, load cell, and rod used to connect tractor and trailer are shown in Fig. 2 and Fig. 4. The full range of the load cell is ±44 N with signal amplification provided by an RDP Electronics S7DC amplifier. Measurement error encompassing overall repeatability, thermal drift, and non-linearity is estimated at better than ±0.7% (of total model drag) and based on repeated measurements made under the same test conditions. All load data was sampled at 1000 Hz over an interval of two minutes and time-averaged. All forces were obtained in tests separate from wake measurements using hot-wire anemometry. Both initial and final 'wind-off' measurements with the moving ground running were taken and used for data correction. This allowed the influence of the wind to be isolated as recommended in SAE J1252 (SAE International 2012). All measurements were repeated at least three times to assess variability.

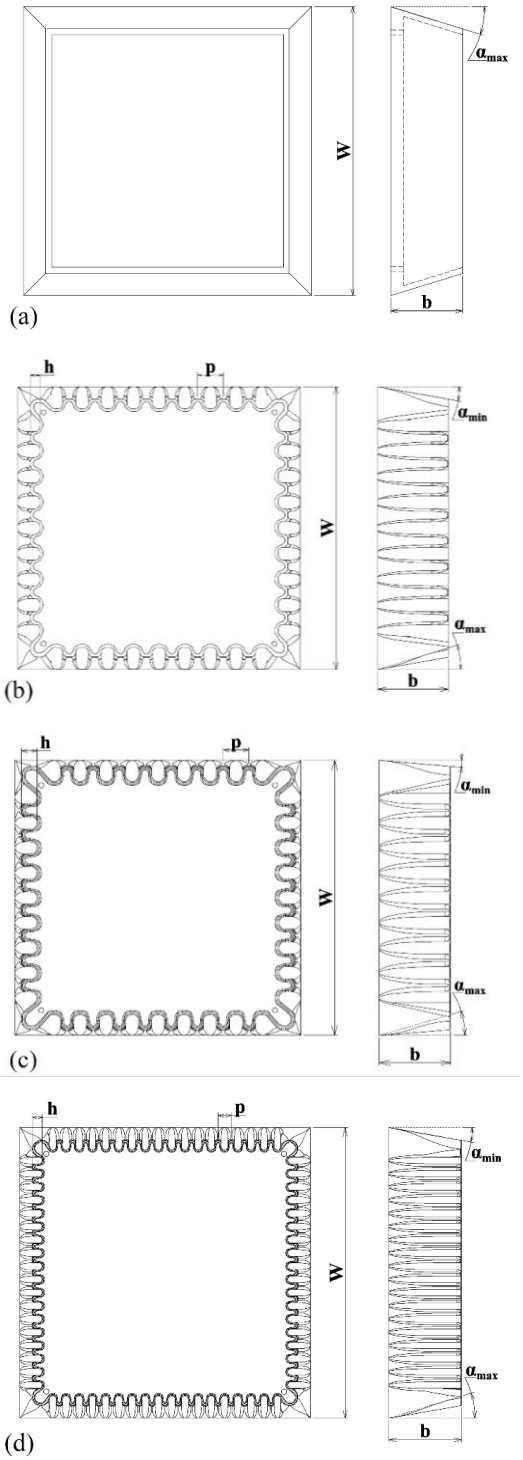


**Fig. 3. Schematic of base inserts: (a) BT; (b) LB1; (c) LB2; (d) LB3.**

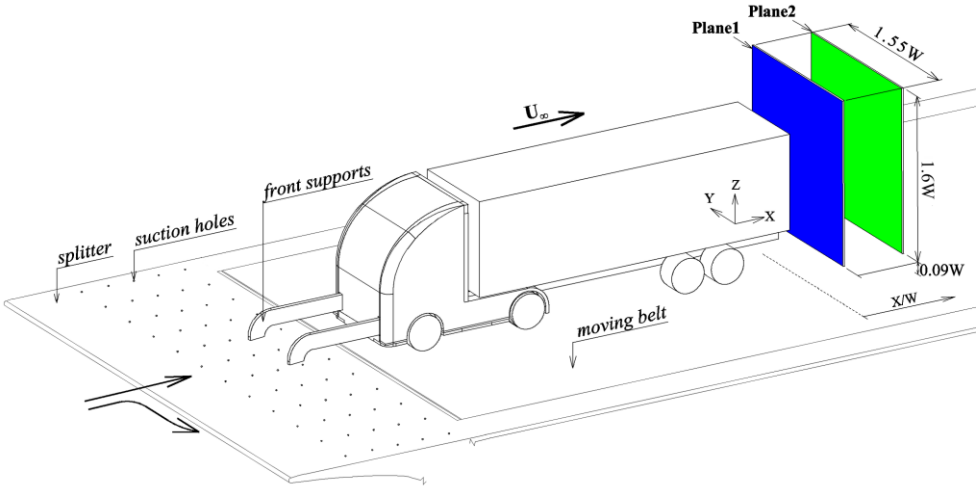


**Fig. 4. Schematic of the model installed in the test section and hot-wire measurement planes used.**

**Table 1 Summary of geometric parameters for the base inserts**

| | b | p | h | $\alpha_{min}$ | $\alpha_{max}$ | β |
|---|---|---|---|---|---|---|
| BT | 0.25W | - | - | - | 17° | - |
| LB1 | 0.25W | 0.091W | 0.034W | 10° | 17° | 3.5° |
| LB2 | 0.25W | 0.091W | 0.056W | 5° | 17° | 6.0° |
| LB3 | 0.25W | 0.045W | 0.034W | 10° | 17° | 3.5° |

**Table 2 Specifications for hot-wire measurement planes**

| | X/W | No. of positions | Position increment |
|---|---|---|---|
| Plane1 | 0.38 | 1365 | 5mm |
| Plane2 | 1.05 | 360 | 10mm |

## 2.5 Hot-Wire Anemometry

The hot-wire apparatus used is a Dantec StreamwarePro. This system is fully integrated and controlled, allowing automated data acquisition. A Dantec P61 dual-sensor probe was used to measure wake velocities in all three axes; X, Y, and Z. The probe was automatically positioned by an Isel 3D traverse system controlled through StreamwarePro software. Probe calibration was performed using a Dantec StreamLine 90H02 Flow Unit, in accordance with the manufacturer's specified procedures (Dantec Dynamics 2000). The overheat ratio used was 0.8 based on the recommendations of Dantec Dynamics (2000), Jørgensen (2002), and Dantec Dynamics (2018). Calibration coefficients were determined using ten, equally-spaced, calibration positions up to a maximum velocity of 40 m/s. Temperature corrections, assessed via the integrated StreamLine temperature probe, were applied to all data.

During testing, all measurements taken at the same position through separate runs were averaged. To assess wake development, velocities were sampled at two different planes (Plane1 and Plane2) for all configurations. The first plane (Plane1) is positioned closest to the baseline model at a distance X/W=0.38 downstream, with Plane2 positioned X/W=0.67 further aft. Corresponding distances downstream with base inserts attached (from trailing edges) were ΔX/W=0.13 and ΔX/W=0.80 respectively. Measurement grid characteristics chosen for analysis are summarised in Table 2 (common width, ΔY/W=1.55, and height, ΔZ/W=1.6) with finer spatial resolutions (grids employing a 2.5mm spacing directly behind the base insert trailing edges) examined for Plane1 achieving similar results to those obtained. For Plane2, the number of positions was reduced to better optimise test duration with signal lengths up to 5 sec used for all analyses. All data was sampled at 1000 Hz with a lower limit of 10 mm above the belt surface (see Fig. 4) chosen to minimise the likelihood of probe damage. This lower limit is

hereafter designated Z/W=0.09 with Y/W=0 corresponding to the tunnel centreline. Mean data convergence was assessed using up to 10000 samples (10 sec). Velocity convergence to within 1% was achieved after 1800 samples. For each plane, data is presented interpolated by a factor of two (using Gaussian process regression) to enhance feature resolution. Uncertainties in velocity and vorticity magnitudes are lower than ±1 m/s and $\Delta\Omega$ = ±0.05 respectively.

## 3. Results And Discussion

### 3.1 Trailer Drag

Figure 5 presents the percentage change in baseline total drag coefficient ($C_D$ = 0.72) measured acting on the trailer for the BT and LB1-3. It is clear that all lobed boat-tails perform better than the BT. Lobed Boat-tail 1 produced the highest drag reduction at 10.2%, although LB2 (reduction of 9.6 ± 0.7%) resides within stated experimental uncertainty. Among the lobed boat-tails, LB3 provided the smallest drag benefit at 8.8%, however, remained significantly more effective than the standard BT configuration with a 6.9% reduction. These results show, in all cases, the addition of lobed mixing profiles to be an effective means of enhancing drag reduction compared to a standard BT. Also notable is the influence of lobe pitch and height, with decreasing pitch (LB1 and LB3) and increasing height (LB1 and LB2) seen to marginally degrade performance; the optimum is likely near LB1. The combination of minimum pitch and height (LB3) produced the lowest drag benefit with this trend ($p\rightarrow0$, $h\rightarrow0$) suggesting further reductions would approach the drag reduction of the BT. Given the ability of all lobed profiles to further enhance drag reduction, it seems that integration onto existing boat-tails (for added benefit), or their application to less ideal, more extreme BT configurations, with the same overall aerodynamic benefit, may be possible.

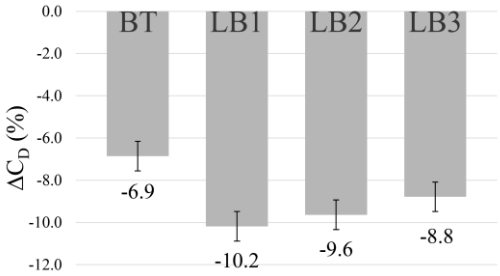


**Fig. 5. Measured total drag reduction compared to the baseline.**

### 3.2 Wake Measurements

Results from wake measurements for the five configurations tested are shown in Figs. 6-15. Figure 6 presents streamwise velocity magnitude contours in the baseline wake at both measurement planes. At first inspection, undisturbed freestream flow can be seen surrounding the model in both planes apart from near the moving ground on both sides of the model (|Y/W|>0.5 for Z/W<0.2). These areas correspond to remnants of the upstream boundary layer with $U/U_\infty\approx0.9$. Given the distance to the base inserts, and $U/U_\infty\approx1$, these elements are not expected to influence significantly comparative performance.

Within the wake, lower velocity magnitude contours pervade its centre and indicate a strong correlation to results observed previously at similar scale (Lo and Kontis 2017; Castelain *et al.* 2018). At X/W=0.38 (Fig. 6(a)) wake size remains near-co-incident with model cross-section, being near-symmetric vertically (about Y/W=0), but asymmetric horizontally (mid-plane at Z/W=0.71). Results from Mason and Beebe (1978) show similar trends, as do McArthur *et al.* (2016) who attribute the horizontal asymmetry to the disparate size and locations of upper and lower wake vortices. Below Z/W≈0.45, velocity magnitude remains marginally higher ($U/U_\infty\approx0.5$) than that within the base wake (|Y/W|<0.5, 0.45<Z/W<1.4). This is known to be a consequence of exposure to exiting underbody flow and is in general agreement with Castelain *et al.* (2018). Across the trailer base, wake velocity magnitudes appear distributed uniformly with a decrease typical from the top towards the ground until the minimum registered ($U/U_\infty\approx0.18$ within 0.55<Z/W<0.8, |Y/W|<0.4 - Note need be made that hot-wire anemometry is unable to always measure accurately within recirculating flows, however, this does not preclude direct comparison as an identical calibration, and test methodologies, were used between configurations). At X/W=1.05 (Fig. 6(b)), the vertical symmetry and horizontal asymmetry are preserved. At this position, the vertical wake size (defined here as encompassing $U/U_\infty<0.8$) remains relatively unchanged compared to X/W=0.38, as does the lateral wake size above Z/W>0.8. However, below this region Z/W<0.8, wake size shows a reduced width (from |Y/W|<0.5 to |Y/W|<0.4). This area highlights the strongest streamwise velocity gradients which extend to ground level. Lowest measured wake velocity magnitudes ($U/U\infty<0.4$) are found within this narrower region, with some evidence of these areas also stretching vertically (0.1<Z/W<1.3) compared to X/W=0.38.

To better interrogate areas of strong flow rotation, Fig. 7 provides topologies of crosswise ($\Omega_Y$) and heightwise ($\Omega_Z$) vorticity for the baseline (Note - $\Omega Y$ and $\Omega Z$ were calculated and used for comparison without any X-direction component and results within $-1.5<\Omega Y<4$ – Fig. 7(a), and $-4<\Omega Z<4$ – Fig. 7(b) have been omitted to aid clarity). As shown, maximum $\Omega_Y$ and $\Omega_Z$ occur in regions where flow separation from the trailer base results in high velocity gradients and fluctuations (top and side shear layers). This is manifested principally via the fixed separation in this region and compares with both McArthur *et al.* (2016) and Lo and Kontis (2017). From Fig. 7(b), $\Omega_Z$ indicates near-symmetry about Y/W=0 with no significant maximum

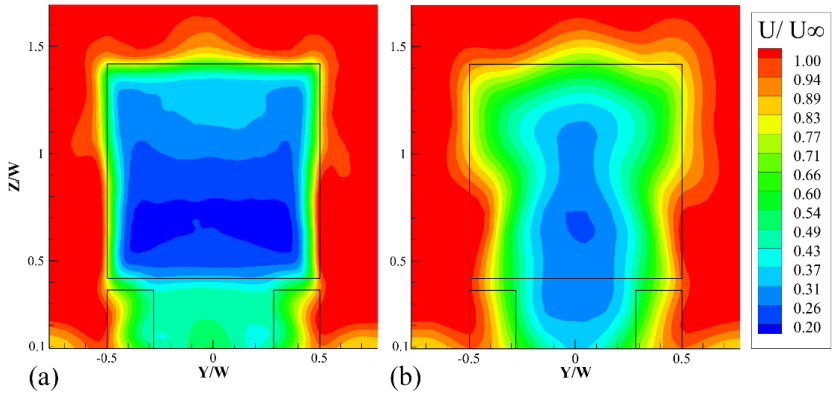


**Fig. 6. Streamwise velocity contours within the Baseline wake: (a) X/W=0.38, (b) X/W=1.05.**

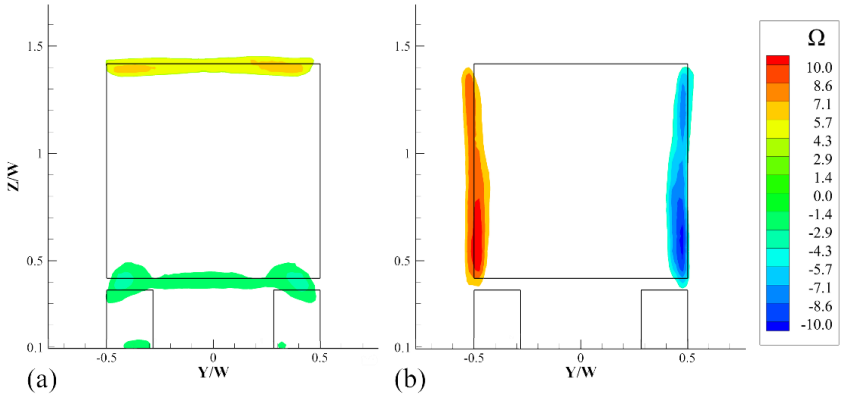


**Fig. 7. Baseline wake vorticity for X/W=0.38: (a) $\Omega_Y$, (b) $\Omega_Z$ (results -1.5<$\Omega_Y$<4 and -4<$\Omega_Z$<4 omitted).**

magnitude disparity ($\Omega_{Zmax}$ ≈|10|). As expected, $\Omega_Y$ shows no such similitude with higher magnitudes ($\Omega_{Ymax}$ ≈|6.7|) along the top (1.35<Z/W<1.45) and lower ($\Omega_{Ymax}$ ≈|3.7|) nearer ground level (0.3<Z/W<0.5); a consequence of the higher velocity underbody flow. Considered further, Fig. 7(a) also indicates crosswise vorticity along the top edge strongest close to the sides (0.3<|Y/W|<0.5 at Z/W≈1.4) relative to the midsection (|Y/W|<0.3). This result is most likely representative of the higher velocity gradients there (i.e. see Fig. 6(a)). Similar flow rotation, but more pronounced ($\Omega_{Zmax}$ ≈|10|), is observed at both sides (|Y/W|≈0.5 between 0.4<Z/W<0.85) in Fig. 7(b). Comparing this figure to Fig. 7(a), strongest vorticity appears at these positions, providing some explanation for the observed wake contraction below Z/W≈0.8 (see Fig. 6(b)).

### 3.3 Influence of Standard Boat-Tail Insert

Given well correlated trends for the baseline results exist, results for the BT are now considered. From Fig. 8(a), one immediate implication of adding this insert is a reduction in wake size; from the top towards the vehicle centreline (ΔZ/W≈0.1) and inboard from the sides (ΔY/W≈0.1). Shear layers now reside closer to the BT trailing edges with this influence identified previously as a result of adding boat-tails (Altaf *et al.* 2014; Kehs *et al.* 2013). The influence of the flow transitioning from the narrower boat-tail end to the wider ground flow is particularly evident, with a larger, lower wake (0.1<Z/W<0.6, |Y/W|<0.6) shown in Fig. 8(a). Comparisons to Fig. 6(a), also show minimum velocity magnitudes to displace vertically into the upper region with the BT added (0.7<Z/W<1.3 – Fig. 8(a)), with comparatively lower, more distributed magnitudes (0.5<Z/W<1.35, |Y/W|<0.4); a consequence of the trapped cavity flow. At X/W=1.05 (Fig. 8(b)), higher velocity magnitudes (0.45<U/U∞<0.7 within 0.7<Z/W<1.25, |Y/W|<0.3) are seen directly behind the BT base with stronger crosswise and heightwise wake contractions compared to Fig. 6(b). Two important implications can be inferred from this behaviour. Firstly, with higher surrounding velocity magnitudes, lower static pressures can be inferred (lower pressure recovery), inhibiting further drag reduction (Tombazis and Bearman 1997; Park *et al.* 2006). Secondly, the upper wake structure is nearer closure, quite distinct from the lower velocity magnitudes, wider wake, nearer ground level (Z/W<0.5). This latter effect is quite pronounced, with an increase of ΔY/W≈0.3 relative to the baseline (Fig. 6(b)). Lowest velocity magnitudes (U/U∞≈0.23) now reside in this region (0.2<Z/W<0.5, |Y/W|<0.2) relocating from 0.55<Z/W<0.75, |Y/W|<0.1 (Fig. 6(b)). This low velocity magnitude region, previously positioned to act beneficially to enhance trailer drag reduction for the baseline (lower wake velocities produce

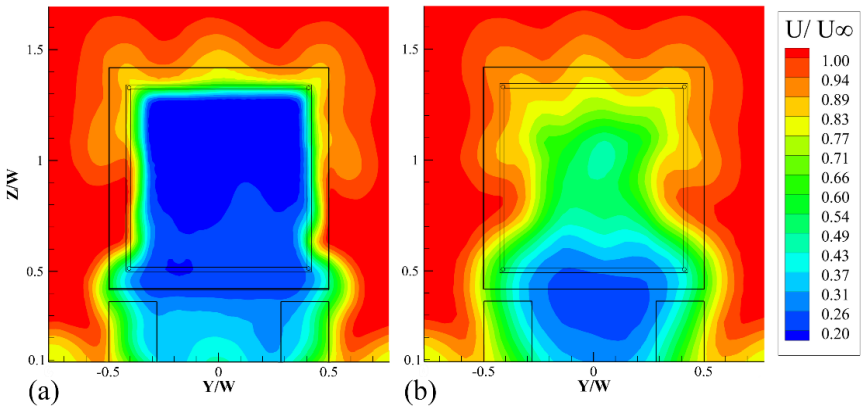


**Fig. 8. Streamwise velocity contours within the BT wake: (a) X/W=0.38, (b) X/W=1.05.**

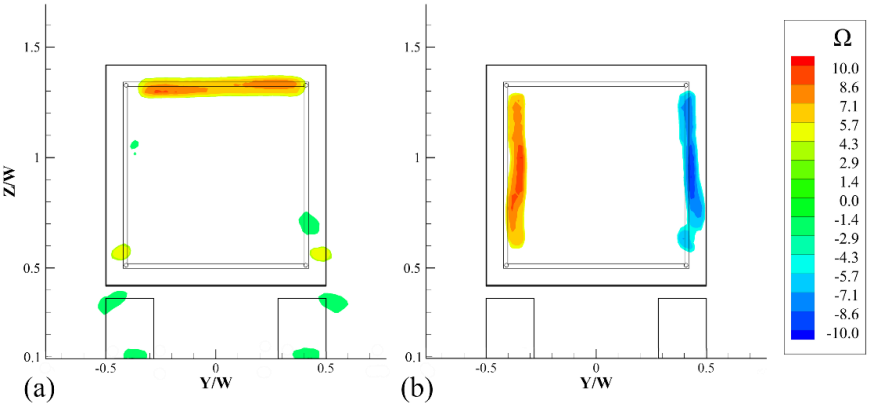


**Fig. 9. BT wake vorticity for X/W=0.38: (a) $\Omega_Y$, (b) $\Omega_Z$ (results -1.5<$\Omega_Y$<4 and -4<$\Omega_Z$<4 omitted).**

higher pressures), now acts more ineffectually on the trailer base for the BT (moved lower towards the underbody region).

With further comparisons, BT wake vorticity (Fig. 9(a, b)) is noted topologically similar to Fig. 7(a, b), but with spatial reductions (width and height), commensurate with corresponding trailing edge lengths. Distinctly, Fig. 9 shows higher $\Omega_Y$ ($\Omega_{Ymax}$ ≈|9|) along the top edge (1.3<Z/W<1.4), $\Omega_{Ymax}$ ≈|1| along the bottom edge (Z/W=0.4), and similar $\Omega_{Zmax}$ ≈|10| along its sides. Higher vorticity magnitudes along the top, with comparable $\Omega_Z$ at the sides suggests stronger flow entrainment towards the centre of the wake from above.. This is confirmed most clearly by heightwise (towards the ground) and crosswise reductions of the BT wake width shown in Fig. 8(b). For the sides, this influence appears limited below Z/W≈0.7 which corresponds to the lower extent of the side shear layers identified in Fig. 9(b). Lowest velocity magnitudes appear within Z/W<0.4 in agreement with Schaut and Sengupta (2015) who identify the bottom edge isolating this part of the wake, raising the static pressure beneath.

### 3.4 Influence of Lobed Mixers

Figure 10 presents streamwise velocity contours for LB1-3. At X/W=0.38, topologies appear very similar. This is somewhat expected due to the short relative distance to the first measurement plane (ΔX/W=0.13). Consistently, all configurations indicate near-symmetry vertically with the same horizontal asymmetry observed previously. Lowest velocity magnitudes areas reside typically within the cavity (|Y/W|<0.4, 0.4<Z/W<1.3), with a wider lower wake portion (albeit marginally narrower by ΔY/W≈0.1-0.2 compared to Fig. 8(a)) again evident near ground level (0.1<Z/W<0.4).

At X/W=1.05, further comparisons highlight strong transverse wake contractions centred at Z/W≈0.8 absent from previous configurations. This characteristic results in an almost ‘hourglass’ wake topology, showing development of lower wake velocity magnitudes above and below a ‘waist’. The lower wake structure shows generally greater width and lower velocity magnitudes relative to the upper segment, and both the baseline (Fig. 6(b)), and the BT (Fig. 8(b)), at Z/W≈0.6. These findings support the trend shown in Fig. 5, where lower velocity magnitudes indicate greater pressure recovery and, consequently, larger drag reduction ($U/U_\infty$≈0.19 within |Y/W|<0.1, 0.46<Z/W<0.6 for LB1, $U/U_\infty$≈0.19 within |Y/W|<0.1, 0.46<Z/W<0.7 for LB2, and $U/U_\infty$≈0.20 within |Y/W|<0.1, 0.53<Z/W<0.56 for LB3). Above the ‘waist’ (Z/W>0.8) magnitudes are greater with $U/U_\infty$≈0.25 for LB1, $U/U_\infty$≈0.24 for LB2, and $U/U_\infty$≈0.27 for LB3 showing again a good

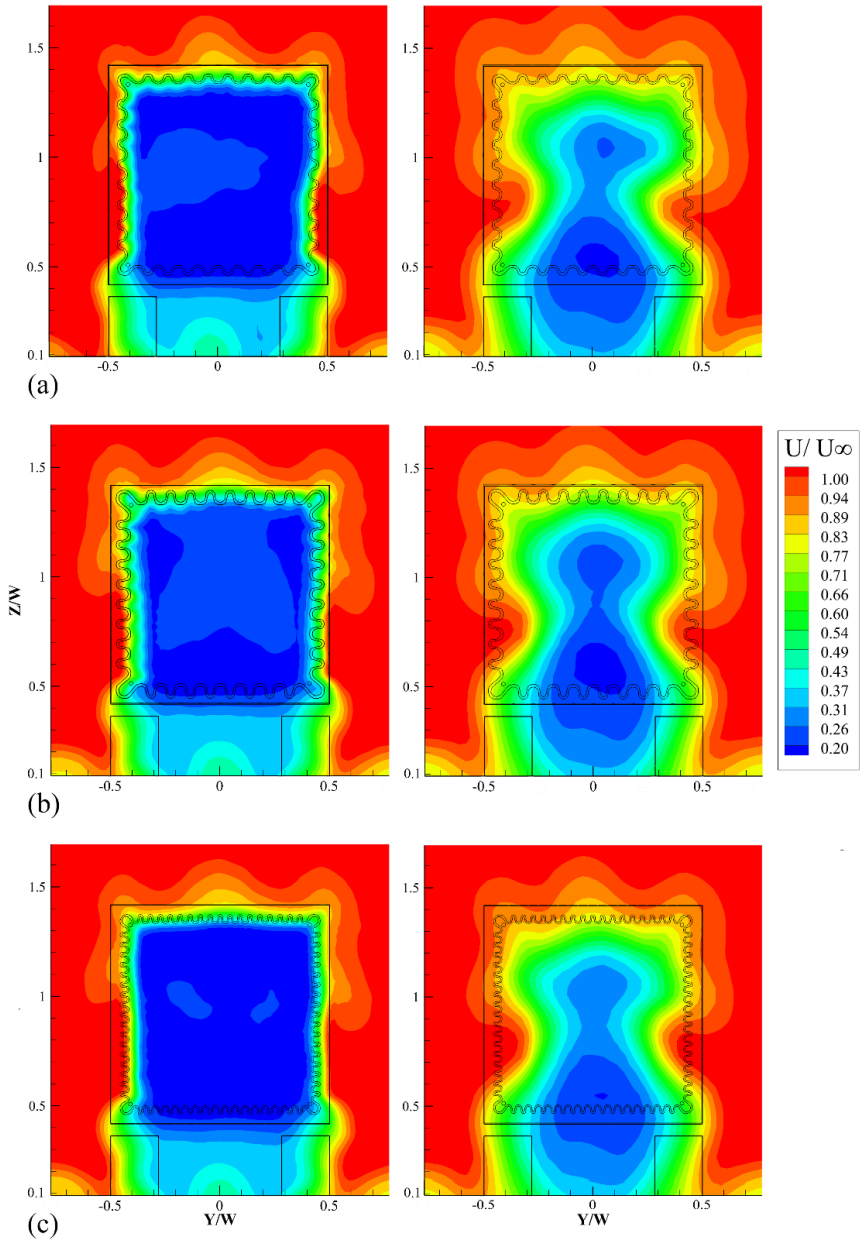


**Fig. 10. Streamwise velocity contours at X/W=0.38 and X/W=1.05: (a) LB1, (b) LB2, (c) LB3.**

correlation to Fig. 5.

Comparing Fig. 10(a-c) at X/W=1.05 to Fig. 8(b) directly, a marked shift in the wake topology occurs with the addition of lobed profiling. Perhaps most obvious is the re-establishment of a higher wake ($U/U^{\infty}<0.5$), similar to that shown for the baseline (Fig. 6(b)). This suggests one influence of adding lobed profiling to a traditional boat-tail is to limit flow entrainment towards the ground. This action is proposed a result of the confining effect imparted by the waist (through enhanced crosswise flow); providing uplift or support against downwards movement. Evidence for this mechanism is presented in Fig. 11 (note the increased scale), which details both $\Omega_Y$ and $\Omega_Z$ for LB1 (LB2 and LB3 omitted for brevity) at X/W=0.38. For this case, while comparable vorticity magnitudes exits along the top edge ($\Omega_{Ymax} \approx|9.3|$), significantly greater (near 50% compared to Fig. 9(b)) $\Omega_Z$ develops at the sides ($\Omega_{Zmax} \approx|15|$). These compare to $\Omega_{Ymax} \approx|11.5|$ and $\Omega_{Zmax} \approx|12|$ for LB2 and $\Omega_{Ymax} \approx|10.6|$ and $\Omega_{Zmax} \approx|11|$ for LB3, highlighting a correlation (when considered in conjunction with Fig. 5) between $\Omega_Z$ production and greatest drag benefit. As $\Omega_{Ymax}$ remains more similar for all cases, less impact on drag reduction is inferred.

### 3.4.1 Streamwise Vorticity

To further understand this behaviour, streamwise vorticity contours ($\Omega_X$) for LB1 and LB3 are

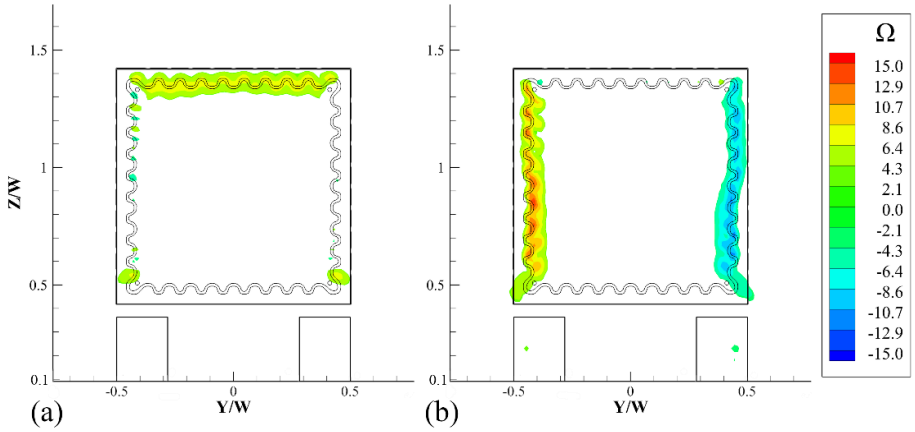


**Fig. 11. Wake vorticity for LB1 at X/W=0.38: (a) $\Omega_Y$, (b) $\Omega_Z$ (results $-4<\Omega_Y<4$ and $-5<\Omega_Z<5$ omitted).**

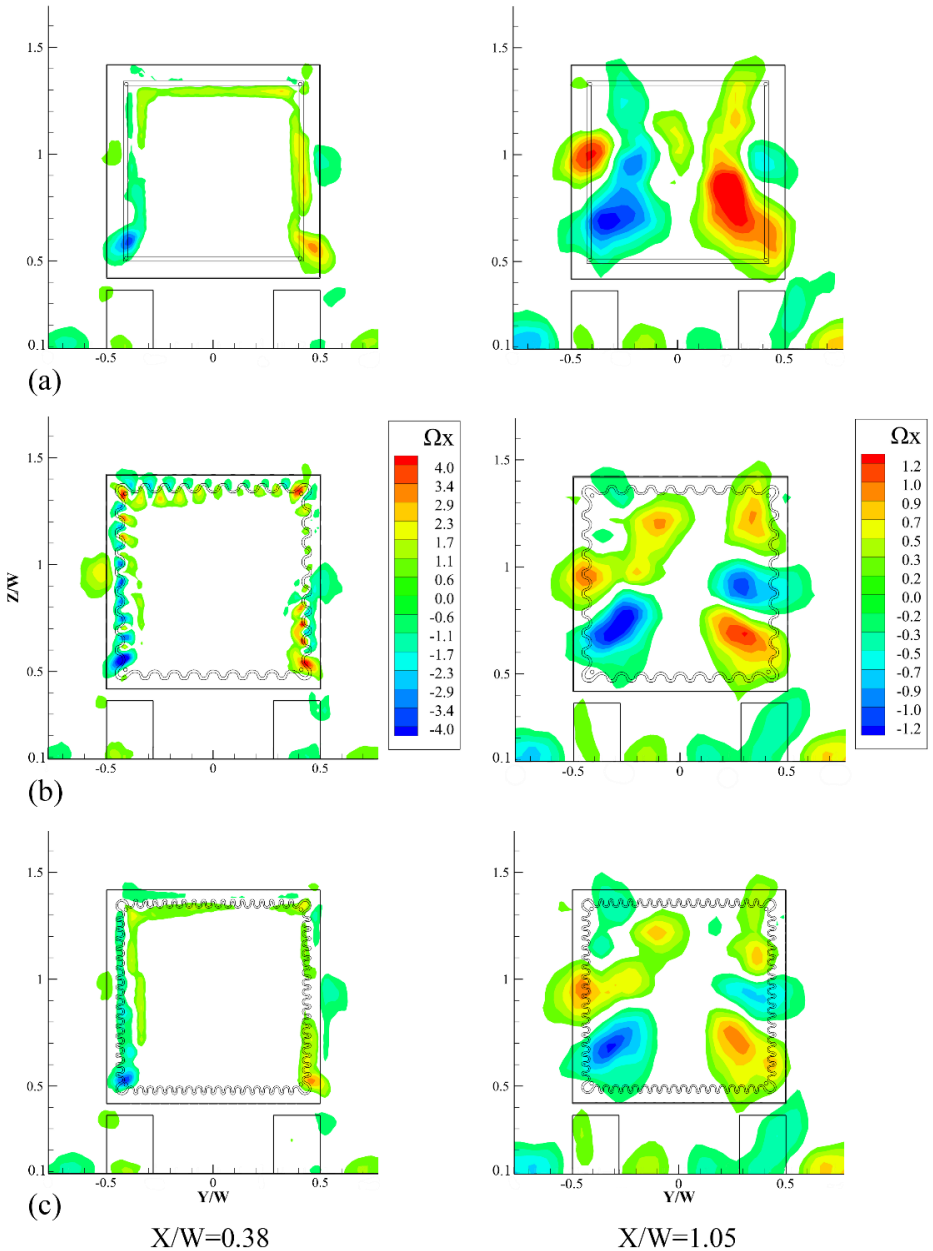


**Fig. 12. Streamwise vorticity contours ($\Omega_X$) at X/W=0.38 and X/W=1.05: (a) BT; (b) LB1; (c) LB3 (results $-0.7<\Omega_X<0.7$ for X/W=0.38 and $-0.2<\Omega_X<0.2$ for X/W=1.05 omitted).**

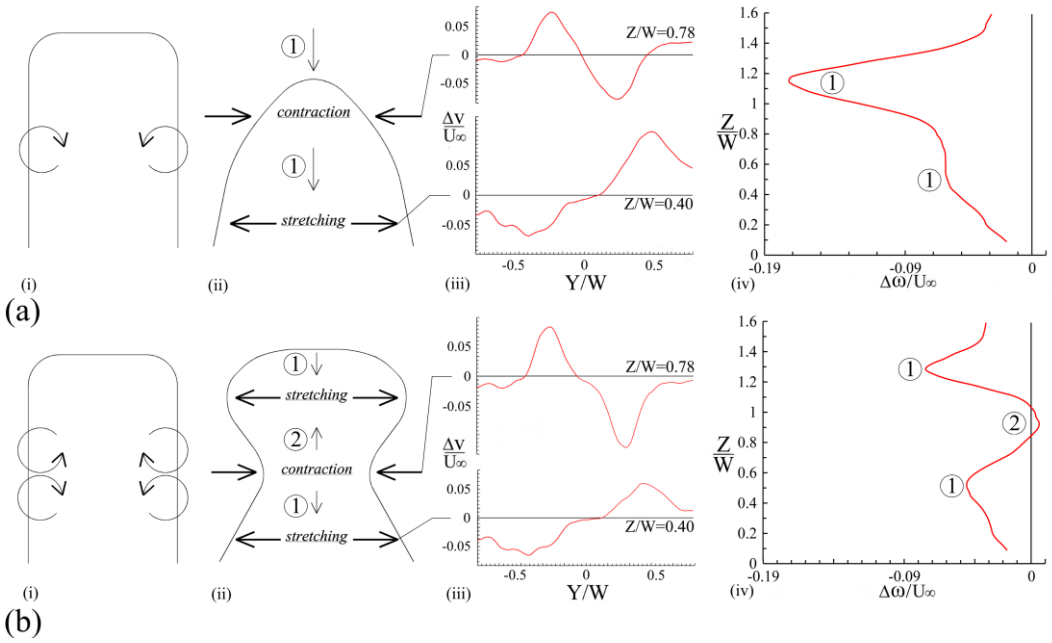


**Fig. 13. Influence of $\Omega_X$ at X/W=1.05 for: (a) BT, and (b) LB1; (i) Schematic of unaltered wake and vortex arrangement, (ii) Inferred influence on wake, (iii) Relative crosswise velocity ($\Delta v/U_\infty$) referenced to Baseline for the BT and LB1 at Z/W=0.40 and 0.78, (iv) Relative heightwise velocity ($\Delta\omega/U_\infty$) referenced to Baseline for BT and LB1 at Y/W=0.**

provided in Fig. 12. Results for the BT are also included for comparison (LB2 omitted due to close similarities to LB1). At first inspection, all results exhibit relatively good vertical symmetry with the possible exception above Z/W=1.1 in Fig. 12(b, c). In these areas, vorticity magnitudes are much weaker, making detection much more challenging. Development of weak co-rotating sets of vorticity at X/W=1.05 are also shown in this region (Y/W=-0.1, Z/W=1.2 and Y/W=0.3, Z/W=1.3 for Fig. 12(b), and Y/W=-0.1, Z/W=1.2 and Y/W=0.4, Z/W=1.1 for Fig. 12(c)) with results presented in Fig. 12(b) at X/W=0.38 indicating the source originates from the top corners of the base (Y/W=-0.45, Z/W=1.35 and Y/W=0.4, Z/W=1.35). Below this level for X/W=0.38, all configurations indicate the generation of pockets of counter-rotating vorticity near the bottom corners of the inserts (0.4<|Y/W|<0.5 at Z/W=0.55). These locations represent the highest magnitudes generated with $\Omega_{Xmax} \approx |3.8|$ for the BT (Fig. 12(a)), $\Omega_{Xmax} \approx |5.8|$ for LB1 (Fig. 12(b) – $\Omega_{Xmax} \approx |6.3|$ for LB2), and $\Omega_{Xmax} \approx |4.2|$ for LB3 (Fig. 12(c)). These findings suggest the bottom corners play a crucial role in streamwise vorticity production. Considering Fig. 12(a) for the BT, concentrations appear most prominent only at this location, with small filaments of elevated $\Omega_X$ aligned along the top (1.3<Z/W<1.4), and side (0.4<|Y/W|<0.5) trailing edges. In comparison, LB1 and LB3 (Fig. 12(b, c)) exhibit more pronounced (particularly LB1) $\Omega_X$ magnitudes at these same locations. Of particular note is LB1 with evidence of small counter-rotating 'cell' pairs at each lobe (Fig. 12(b)). This topology mimics the illustrative streamlines presented in Fig. 1. These cells appear variable in magnitude (most intense near bottom corners) and correlate spatially to the lobed profile; vorticity direction switches at intervals of profile pitch. For each pair, a dominant cell magnitude exists and acts in a direction to entrain flow towards the wake centre (predominantly from the sides). This action supports the crosswise flow enhancement mechanism proposed (and subsequent confining effect imparted by the waist) described in relation to Fig. 10 at X/W=1.05. Measured magnitude comparisons (made at a mid-width position behind the top base edge at X/W=0.38 - $\Omega_X$~1) to those calculated using Eq. (1) also show general agreement. For the LB3 case (Fig. 12(c)) at X/W=0.38, these cells are not clearly visible due to what is believed to be insufficient spatial resolution.

Transition from X/W=0.38 to X/W=1.05 (Fig. 12) indicates that counter-rotating 'cells' generated at X/W=0.38 coalesce into weaker, but larger counter-rotating pairs, centred near base mid-height, at each side. Winant and Browand (1974) observed a similar phenomenon for controlling mixing layer growth; expanding vortices of the same sign tend to undergo a pairing process, with Zaman and Hussain (1980) also showing spatial expansion, coupled with a drop in maximum vorticity result from the same process. For the BT, Fig. 12(a) shows two primary counter-rotating cells centred near |Y/W|≈0.3 at Z/W≈0.7. Situated in close proximity, are induced counter-rotating counterparts (|Y/W|≈0.4 at Z/W≈0.95). Considering maximum magnitudes, the former is dominant ($\Omega_{Xmax} \approx |1.5|$) with their main action being firstly to entrain flow transversely to the wake centre and then downwards towards the ground. This action is represented in Fig. 13(a) with a predominant, vortex-induced contraction, at the top of the wake, and subsequent

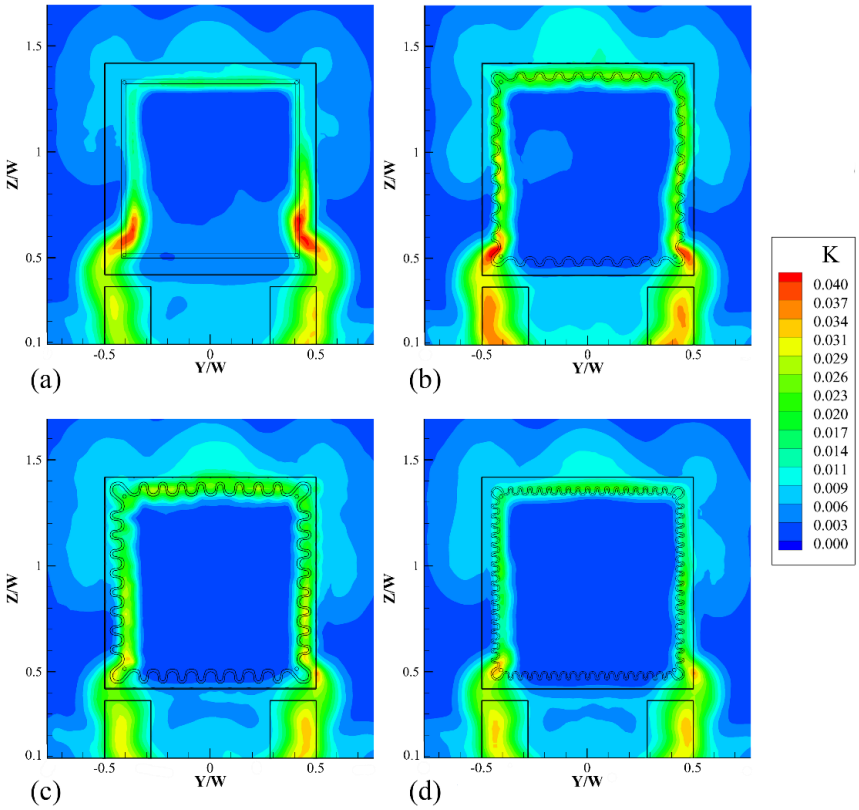


**Fig. 14. Turbulence Kinetic Energy (K) for X/W=0.38: (a) BT, (b) LB1, (c) LB2, (d) LB3.**

expansion, or stretching, nearer the ground. For LB1 and LB3 (includes LB2), a related, but different mechanism occurs. In these instances, two sets (one for each side) of counter-rotating cells, of near equal magnitude ($\Omega_{Xmax} \approx |1.2|$), and similarly located, dominate the wake. These cells induce the same transverse contraction, entraining flow towards the centreline, however, each upper and lower cell also induces stretching at wake top and bottom. Figure 13(b)(ii) highlights this difference. Direct evidence supporting this behaviour is presented in Fig. 13(a-b)(iii). Differences in crosswise flow velocity (referenced to the baseline case) induced by the inclusion of BT and LB1 show both, contraction or relative 'inflow' (at Z/W=0.78), and stretching, or relative 'outflow' closer to the ground (at Z/W=0.4). Figures 13(a-b)(iv) provide further evidence showing similar relative heightwise velocity. As indicated for the BT case, the principle action of the primary vortex pair is entrainment towards the ground (labelled as 1) in agreement with Fig. 13(a)(ii). For LB1, both positive and negative relative heightwise velocities exist. With the addition of LB1, downward entrainment pervades nearer the ground (Z/W≈0.4) with a relative magnitude ($-\Delta\omega/U_\infty$) similar to adding the BT. At higher positions however, specifically that co-incident with the 'waist' (Z/W=0.78), a small, relative 'upwash' is indicated (labelled as 2). This action results from the two sets of counter-rotating vortices (of near equal magnitude) providing the 'uplift' to the wake absent for the BT (see Fig. 13(b)(ii)). At higher positions (Z/W>0.78), downward entrainment is again re-established, but at notably lower levels compared to the BT (Fig. 13(a-b)(iv)). Fundamentally, these results demonstrate that the addition of lobed-mixing profiles to a standard BT has the ability to significantly influence the structure of the wake resulting in additional drag benefits.

### 3.4.2 Mixing

To assess any possible enhanced mixing, normalised turbulence kinetic energy (K) is presented in Figs. 14-15 for LB1-3 and the BT. Table 3 also presents plane-averaged K (denoted as $\overline{K}$). At X/W=0.38, all four configurations exhibit similarities; increased K immediately behind base insert top and side trailing edges, the rear wheels, and within the transition region subtending the two. Shown in Fig. 14(a), most intensive K for the BT is centred just above the bottom corners (|Y/W|≈0.4 at Z/W≈0.6) with corresponding LB1-3 indicating slightly lower (Z/W≈0.5). Strong flow mixing exists in these areas. Of equal relevance is elevated K surrounding the top (1.3<Z/W<1.4) and side edges (0.3<|Y/W|<0.5) of the inserts, particularly the affected width. For the BT (and to a lesser extent LB3), lower K acting over thinner regions is typical, with LB1 and LB2 exhibiting higher, more distributed magnitudes in the same areas. Considered holistically, Table 3 confirms the implication of these results; larger $\overline{K}$ for LB1 and LB2 (X/W=0.38) providing direct evidence of enhanced flow mixing due to the lobed profiling. This has been described by Hu *et al.* (2001, 2002),

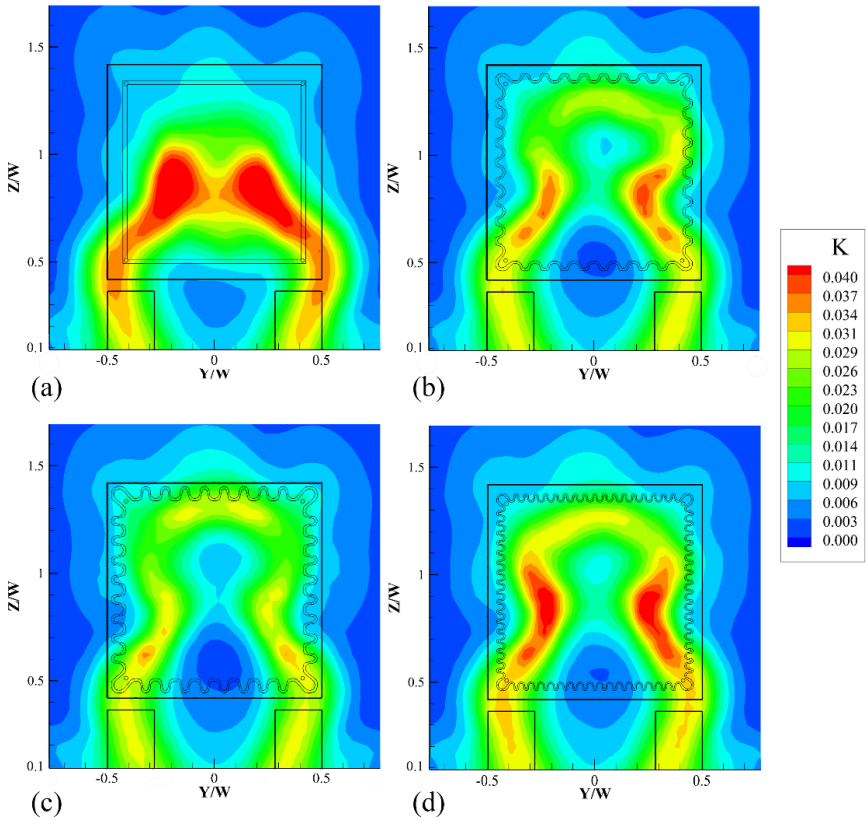


**Fig. 15. Turbulence Kinetic Energy (K) for X/W=1.05: (a) BT, (b) LB1, (c) LB2, (d) LB3.**

**Table 3 Plane-averaged Turbulence Kinetic Energy ($\bar{K}$) for the BT, LB1, LB2, and LB3**

| | BT | LB1 | LB2 | LB3 |
|---|---|---|---|---|
| X/W=0.38 | 0.0064 | 0.0073 | 0.0067 | 0.0058 |
| X/W=1.05 | 0.0124 | 0.0111 | 0.0105 | 0.019 |

Cooper *et al.* (2005) and Mao *et al.* (2006) as a 'stirring' effect produced by large-scale vorticity with these studies also highlighting maximum turbulent mixing occurs within short distances from the trailing edge (X/h<6, where h is the crest-trough height of lobed mixer profile). In these regions, structures break down into smaller elements reducing turbulence growth rate. Beyond X/h>8, K growth also slows (Hu *et al.* 2001) with the reverse true for unmodified surfaces; K increases almost linearly up to X/h≈11. Results presented here (Table 3) support these findings.

At X/W=1.05, similar effects are observed. From Fig. 15, all four inserts exhibit elevated, more distributed K compared to Fig. 14. From Fig. 15(a), the BT indicates substantially higher, more concentrated K, developing near base mid-height. At this streamwise position (equivalent to X/h≈23.7 for LB1 and X/h≈14.2 for LB2), LB1 and LB2 show the lowest K demonstrating the same enhanced mixing mechanisms exist for this application as others already identified. Also of interest are the areas of maximum K situated at the 'waist' (Z/W≈0.78) position for LB1-3 (Fig. 14(b-d)) and that of more elevated K near the top (Y/W≈0, Z/W≈1.3). McCormick and Bennett (1994) and Yu and Yip (1997) observed similar results near the 'pinch-off' position, together with Mao *et al.* (2006), who identify highest K near the top, where stretching is the most.

## 4. CONCLUSION

The use of lobed mixers as an effective means for enhancing drag reduction of boat-tailed ground vehicles has been demonstrated. Experimental tests were conducted at a Reynolds number (based on vehicle width) of $Re_W = 2.3 \times 10^5$ on a $1/24^{th}$-scale model, representative of a Heavy Goods Vehicle. The test setup involved the influence of a moving ground.

All lobed-mixing geometries tested were found to

provide additional drag benefits compared to both a baseline (no device) and legacy boat-tail. The best drag reduction achieved was 10.2 ± 0.7% from the baseline. Assessment of changing lobed profile pitch and height found that reducing pitch, and increasing height (within experimental uncertainty) degrade performance. From detailed wake measurements, the principle mechanism responsible for the increased drag reduction observed was the production of additional vorticity at the side lobes, which enhanced crosswise flow, limiting wake entrainment towards the ground. This action results in a spatially higher wake of reduced velocity magnitudes, with a characteristic 'waist'. Relative transverse wake contraction and stretching together with relative downwash and upwash velocity components were also identified as responsible for fundamentally modifying the wake to produce an 'hourglass' topology. Within the wake, lobed profiling was also observed to be an effective means to enhance mixing, in agreement with results obtained in other literature on similar geometries.

## ACKNOWLEDGEMENTS

This project is supported by the EPSRC Doctoral Training Program. The financial support of Brunel University along with the assistance provided by technical staff is also acknowledged.

## REFERENCES

Altaf, A., A. A. Omar and W. Asrar (2014). Passive drag reduction of square back road vehicles. *Journal of Wind Engineering and Industrial Aerodynamics*. *Elsevier* 134,30–43.

Bolgar, I., S. Scharnowski and C. J. Kähler (2016). Control of the reattachment length of a transonic 2D backward-facing step flow. *Springer Proceedings in Physics* 185(June), 241–248.

Butcher, L. (2009). Lorry sizes and weights. *House of Commons SN/BT/654*.

Castelain, T., M. Michard, M. Szmigiel, D. Chacaton and D. Juve (2018). Identification of flow classes in the wake of a simplified truck model depending on the underbody velocity. *Journal of Wind Engineering and Industrial Aerodynamics* 175(September 2017), 352–363.

Cooper, K. R. (2003). Truck Aerodynamics Reborn – Lessons from the Past. *SAE Technical Paper* (2003-01–3376).

Cooper, N. J., P. Merati and H. Hu (2005). Numerical simulation of the vortical structures in a lobed jet mixing flow. *43rd AIAA Aerospace Sciences Meeting and Exhibit - Meeting Papers* 13455–13467.

Dantec Dynamics (2000). *StreamLine/StreamWare - Installation and User's Guide Vol. 2*. Dantec Dynamics.

Dantec Dynamics (2018). *Hot-wire & Hot-film Probe Usage Recommendations.* Dantec Dynamics.

Department for Transport UK (2017a). *Road Traffic Estimates: Great Britain 2016*.

Department for Transport UK (2017b). *Table RFS0141: Fuel consumption by type and weight of vehicle: annual 2004 - 2016*.

Depuru Mohan, N. K., K. R. Prakash and N. R. Panchapakesan (2015). Mixing Augmentation by Multiple Lobed Jets. *American Journal of Fluid Dynamics* 5(2), 55–64.

Duriez, T., J.-L. Aider and J. E. Wesfreid (2006). *Base flow modification by streamwise vortices. Application to the control of separated flows.*, *Proceedings of FEDSM2006*. Miami, FL.

Grover, K. and K. D. Visser (2006). Over-the-Road Tests of Sealed Aft Cavities on Tractor Trailers. *SAE Technical Paper*, (724).

Howard, F. G. and W. L. Goodman (1985). Axisymmetric bluff-body drag reduction through geometrical modification. *Journal of Aircraft* 22(6), 516–522.

Howell, J., D. Sims-Williams, A. Sprot, F. Hamlin and R. Dominy (2012). Bluff Body Drag Reduction with Ventilated Base Cavities. *SAE International Journal of Passanger Cars - Mechanical Systems* 152–160.

Hu, H., T. Saga, T. Kobayashi and N. Taniguchi (2001). A study on a lobed jet mixing flow by using stereoscopic particle image velocimetry technique. *Physics of Fluids* 13(11), 3425–3441.

Hu, H., T. Saga, T. Kobayashi and N. Taniguchi (2002). Mixing process in a lobed jet flow. *AIAA Journal* 40(7), 1339–1345.

Hucho, W. H. and G. Sovran (1993). Aerodynamics of Road Vehicles. *Annual Review of Fluid Mechanics*, 25, 485–537.

ICBE (2018). *tCO2 in Gaseous Volume and Quantity of Fuel Type*. http://www.icbe.com/carbondatabase/volumeconverter.asp

Jørgensen, F. E. (2002). *How to measure turbulence with hot-wire anemometers - a practical guide*. *Dantec Dynamics* 3244.

Kehs, J. P., K. D. Visser, J. Grossman, J. Niemiec, A. Smith and C. M. Horrell (2013). A Comparison of Full Scale Aft Cavity Drag Reduction Concepts With Equivalent Wind Tunnel Test Results. *SAE International Journal of Commercial Vehicles* 486–497.

Krajnović, S. and L. Davidson (2005). Influence of

floor motions in wind tunnels on the aerodynamics of road vehicles. *Journal of Wind Engineering and Industrial Aerodynamics* 93(9), 677–696.

Lanser, W. R., J. C. Ross and A. E. Kaufman (1991). Aerodynamic performance of a drag reduction device on a full-scale tractor/trailer. *Aerospace Technology Conference and Exposition*.

Lav, C. (2013). Three Dimensional CFD Analysis on Aerodynamic Drag Reduction of a Bluff Tractor Trailer Body using Vortex Generators. *2013 Commercial Vehicles Engineering Congress*, p. 10.

Lo, K. H. and K. Kontis (2017). Flow around an articulated lorry model. *Experimental Thermal and Fluid Science* 82, 58–74.

Mao, R., S. C. M. Yu, T. Zhou and L. P. Chua (2009). On the vorticity characteristics of lobe-forced mixer at different configurations. *Experiments in Fluids* 46(6), 1049–1066.

Mao, R. H., S. C. M. Yu and L. P. Chua (2006). Kelvin - Helmholtz and Streamwise Vortices in the Near Wake of a Single-Lobe Forced Mixer. *Proceedings of the Institution of Mechanical Engineers, Part G: Journal of Aerospace Engineering* 220(4), 279–298.

Martín-Alcántara, A. E., Sanmiguel-Rojas, C. Gutierrez-Montes and C. Martinez-Bazan (2014). Drag reduction induced by the addition of a multi-cavity at the base of a bluff body. *Journal of Fluids and Structures*. *Elsevier* 48, 347–361.

Mason, W.T., J. and Beebe, P. S. (1978). 'The Drag Related Flow Field Characteristics of Trucks and Buses' in Sovran, G., Morel, T., and Mason, W. T., J. (eds) *Aerodynamic Drag Mechanisms of Bluff Bodies and Road Vehicles*. New York-London: Plenum Press, pp. 45–93.

McArthur, D., D. Burton, M. Thompson and J. Sheridan (2016). On the near wake of a simplified heavy vehicle. *Journal of Fluids and Structures*. *Elsevier* 66, 293–314.

McCormick, D. C. and J. C. J. Bennett (1994). Vortical and turbulent structure of a lobed mixer free shear layer. *The American Institute of Aeronautics and Astronautics Journal* 32(9), 1852–1859.

Pankajakshan, R., C. Hilbert and D. Whitfield (2010). Passive Devices for Reducing Base Pressure Drag in Class 8 Trucks in Dillmann, A. and Orellano, A. (eds). *The Aerodynamics of Heavy Vehicles III*. Potsdam 227–235.

Park, H., D. Lee, W. P. Jeon, S. Hahn, J. Kim, J. Kim, J. Choi and H. Choi (2006). Drag reduction in flow over a two-dimensional bluff body with a blunt trailing edge using a new passive device. *Journal of Fluid Mechanics*, 563, 389–414.

Paterson, R. W., M. J. Werle and W. M. Presz (1989). Projectile with Reduced Base Drag (US4813635). United States.

Pujals, G., S. Depardon and C. Cossu (2010). Drag reduction of a 3D bluff body using coherent streamwise streaks. *Experiments in Fluids* 49(5), 1085–1094.

SAE International (2012). *SAE Wind Tunnel Test Procedure for Trucks and Buses (J1252)*. SAE International.

Salati, L., F. Cheli and P. Schito (2015). Heavy Truck Drag Reduction Obtained from Devices Installed on the Trailer. *SAE International Journal of Commercial Vehicles* 8(2), 747–760.

Saltzman, E. and Jr. R. Meyer (1999). *A Reassessment of Heavy-Duty Truck Aerodynamic Design Features and Priorities*. California: NASA National Technical Information Service.

Schaut, N. and R. Sengupta (2015). Aerodynamic Optimization of Trailer Add-On Devices Fully- and Partially-Skirted Trailer Configurations. *SAE International Journal of Commercial Vehicles* 8(2), 2015-01–2885.

Schreyer, A. M. and G. Taskin (2018). Separation Control with Lobe Mixers in the Wake of an Axisymmetric Space-Launcher Model. *New Results in Numerical and Experimental Fluid Mechanics XI*, 315–325.

Skebe, S., R. Paterson and T. Barber (1988). Experimental investigation of three-dimensional forced mixer lobe flow fields. *1st National Fluid Dynamics Conference*. American Institute of Aeronautics and Astronautics (Fluid Dynamics and Co-located Conferences).

Smith, L. L., A. J. Majamaki, I. T. Lam, O. Delabroy, A. R. Karagozian, F. E. Marble and O. I. Smith (1997). Mixing Enhancement in a Lobed Injector. *Physics of Fluids* 9(3), 667–678.

Storms, B. L., J. C. Ross, J. T. Heineck, S. M. Walker, D. M. Driver and G. G. Zilliac (2001). *An experimental study of the ground transportation system (GTS) model in the NASA Ames 7-by 10-ft wind tunnel*.

Strachan, R. K., K. Knowles and N. J. Lawson (2007). The vortex structure behind an Ahmed reference model in the presence of a moving ground plane. *Experiments in Fluids* 42(5), 659–669.

Van Raemdonck, G. and M. van Tooren (2010). 'Numerical and Wind Tunnel Analysis

Together with Road Test of Aerodynamic Add-Ons for Trailers' in Dillmann, A. and Orellano, A. (eds) *The Aerodynamics of Heavy Vehicles III*. Potsdam: Springer International Publishing 237–252.

Waitz, I. A.,Y. J. Qiu, T. A. Manning, A. K. S. Fung, J. K. Elliot, J. M. Kerwin, J. K. Krasnodebski, M. N. O'Sullivan, D. E. Tew, E. M. Greitzer, F. E. Marble, C. S. Tan and T. G. Tillman (1997). Enhanced mixing with streamwise vorticity. *Proy. Aerospace Sci* 33, 323–351.

Winant, C. D. and F. K. Browand (1974). Vortex pairing: The mechanism of turbulent mixing layer growth. *Journal of Fluid Mechanics* 63, pp. 237–255.

Wood, R. M. (2006). A Discussion of a Heavy Truck Advanced Aerodynamic Trailer System. *SOLUS-Solutions and Technologies LLC*.

Yu, S. C. M. and T. H. Yip (1997). Measurements of velocities in the near field of a lobed forced mixer trailing edge. *The Aeronautical Journal - Royal Aeronautical Society* 101(2165), 121–129.

Zaman, K. B. M. Q. and A. K. M. F. Hussain (1980). Vortex pairing in a circular jet under controlled excitation. Part 1. General jet response. *Journal of Fluid Mechanics* 101(3), pp. 449–491.